Current Distribution in PEM Fuel Cells. Part 2: Air Operation and Temperature Effect

Dilip Natarajan and Trung Van Nguyen
Dept. of Chemical and Petroleum Engineering, University of Kansas, Lawrence, KS 66045

DOI 10.1002/aic.10577
Published online June 27, 2005 in Wiley InterScience (www.interscience.wiley.com).

The effect of air flow rate, fuel and oxidant gas stream humidity, and cell operating temperature on the spatial and temporal current density distribution was investigated in a single gas channel PEM fuel cell using a segmented electrode/current collector assembly. Related studies on oxygen operation and fuel starvation effects are presented in part one of this paper. The current density distribution was found to be a strong function of the available oxygen concentration down the channel that was determined by the air supply rate. Higher flow rates reduced the drop in the current density profile along the channel. At lower air flow rates, a simultaneous increase in cell temperature and anode humidification level resulted in increasing segment performance near the inlet accompanied by a related decrease in the current densities downstream. Further increasing the air flow rate ultimately led to enhanced reaction rates over the entire length of the channel. If cell temperature elevation were not accompanied by a corresponding increase in the anode humidification level, the dehydration pattern on the anode side tended to dominate the local current density distribution. Beyond a certain point the current density distribution along the channel was exclusively dependent on oxidant availability and gas diffusion rates and thus neither higher anode humidification nor cell temperature elevation had a significant influence at the chosen operating segment potential. © 2005 American Institute of Chemical Engineers *AIChE J,* 51: 2599–2608, 2005
Keywords: PEM fuel cells, conventional gas distributor, spatial and temporal current density distribution, segmented electrode, air operation

Introduction

Fundamental understanding and alleviation of the various performance and efficiency limiting phenomena in proton-exchange membrane (PEM) fuel cells, with the ultimate goal of fuel cell commercialization, have been the primary focus of research efforts in this area over the past decade. The distribution of local current density at a given cell voltage that is representative of the reaction rate over the active area is the most sought after information for fuel cell performance optimization. The spatiotemporal distribution of the local current density is a function of the reactant and product distribution and their effect on material properties such as membrane conductivity. Because of the small thickness and extreme aspect ratios of the electrodes, consisting of the gas diffusion layer (GDL) and catalyst layer (CL), experimental measurement of species distribution is very difficult. Thus elaborate multiphase, multidimensional mathematical models have been developed in the past to provide such information.[1-11] However, several relevant component properties such as electrode gas and liquid permeability and capillary pressure dependency on liquid water saturation are not available and are usually estimated by fitting the model results to experimental data in terms of average cell current density vs. cell potential. The predictive capability of these models can be improved through more accurate estimates of material properties and model validation that can be achieved only when the simulated results are matched with experimental data on the spatiotemporal local current density

Correspondence concerning this article should be addressed to T. V. Nguyen at cptvn@ku.edu.

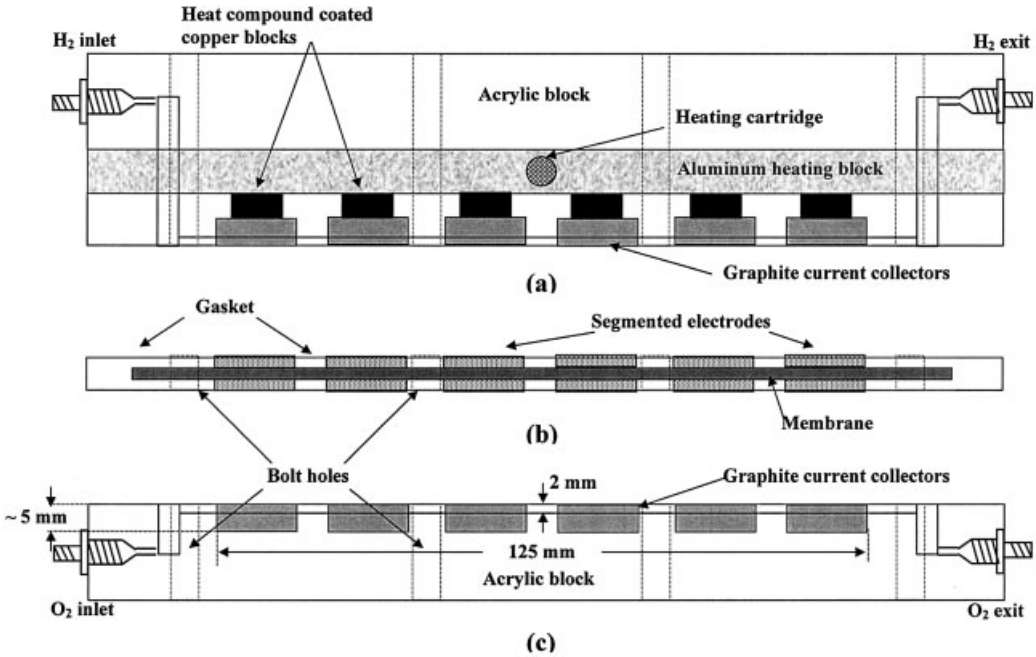

Figure 1. Side view of the segmented fuel cell assembly.

(a) Segmented anode with heating block and acrylic end plate, (b) segmented MEA, and (c) segmented cathode.

distribution. To generate such information, segmented fuel cell assemblies are needed to independently investigate the reaction rate across the active area.

Over the past few years researchers have addressed issues regarding fabrication of such segmented fuel cells and methodology of current distribution measurements. Cleghorn et al.[12] conducted the first current density distribution measurements, where they used printed circuit board (PCB) technology to fabricate fuel cell assemblies with segmented current collectors/flow field. Stumper et al.[13] evaluated three different approaches to map current density distribution. These pioneering approaches to measure local current density distribution have been further refined by other researchers.[14-21] The refinements include segmenting the electrode along with the current collectors, segmentation on both sides (that is, the anode and cathode), and independent control of the segments using a multichannel potentiostat/galvanostat. For the sake of brevity, the reader is referred to the original literature for more information. A detailed review of the literature regarding current density distribution measurements is also available in the first part of this article and in this authors' previous publication.[21]

Most of the cited literature deals with the issue of how to conduct experiments that yield spatial and temporal current density distribution, whereas actual experimental data are limited. The objective of this work was to exploit the tremendous potential of segmented fuel cell in providing spatiotemporal local current density distribution over a wide range of operating variables. Twenty-five experiments were conducted as a part of this study. The first nine experiments dealt with local current density measurements while using oxygen as the oxidant in the cathode and under fuel (hydrogen) starvation conditions. These results are presented in the first part of this article, whereas results from air operation and the effect of cell temperature are addressed here.

Experimental

The fabrication of the various components of the segmented fuel cell assembly (see Figure 1), the segmented membrane electrode assembly (MEA), and the test procedure are described in detail in the first part of this series and, for the sake of brevity, are not repeated here. Three MEAs were fabricated for this study. Results from MEA 1 and MEA 2 are presented in the earlier article, whereas air operation and temperature studies conducted on MEA 3 are presented here. In MEA 3, the anode and cathode had six 7×15-mm segments placed laterally along the length of the channel, giving a total reactive area of 6.3 cm^2.

Table 1 summarizes the experiments that are discussed herein. The numbers reported as cell temperature in Table 1 reflect the measured temperature at one of the cathode segments. The corresponding anode temperatures for the three cell temperatures reported here were 30–31, 47–48, and 58–60°C, respectively. The segment-to-segment variation in temperature on either side was within the accuracy (± 1°C) of the T-type thermocouple.

In run 10, MEA 3 was subjected to multiple potentiostatic staircases between 0.8 and 0.65 V to massage and hydrate the membrane and to evaluate the uniformity in the discharge characteristics of the six electrode segments. The step size was 50 mV and the segments were held at each potential for 5 min. Pure oxygen was used in this massage experiment and the gas flow rates and sparger temperatures are provided in Table 1. The data from the last potentiostatic cycle are provided in Figure 2 in the form of polarization curves for the six segments.

Figure 2 clearly shows remarkable similarity in the performance of the various segments. For instance current densities of the six segments are within 0.01 A/cm^2 at a segment potential of 0.65 V. After massage and uniformity evaluation, runs

Table 1. Summary of Experiments Conducted

Run	Cell T (°C)	H_2 Sparger T (°C)	Air Flow Rate (cm^3/min) (A/cm^2)	Air Sparger T (°C)	Figure	Objectives
10	27–28	40	19 (0.87)*	30	2	Massage and segment evaluation
11	Same as above	Same as above	16.6 (0.16)	Same as above	3	Effect of air flow rate (runs 11–14) and cathode humidification (runs 11, 16, and runs 14, 15) on local current density distribution at lower cell temperature
12	Same as above	Same as above	22 (0.21)	Same as above	4	
13	Same as above	Same as above	35.8 (0.34)	Same as above	5	
14	Same as above	Same as above	47.5 (0.45)	Same as above	6	
15	Same as above	Same as above	Same as above	No sparger	7	
16	Same as above	Same as above	16.6 (0.16)	45	8	
17	44–46	60	Same as above	30	10	Effect of air flow rates (runs 17–19), cathode (runs 19–22) and anode (runs 17, 23 and runs 24, 25) humidification and cell temperature (runs 12, 17, 23–25) on local current density distribution
18	Same as above	Same as above	22 (0.21)	Same as above	11	
19	Same as above	Same as above	35.8 (0.34)	Same as above	12	
20**	Same as above	Same as above	22 (0.21)	50	n/a	
21**	Same as above	Same as above	Same as above	60	n/a	
22	Same as above	Same as above	Same as above	75	13	
23	Same as above	40	Same as above	30	15	
24	54–56	Same as above	Same as above	Same as above	16	
25	Same as above	75	Same as above	Same as above	17	

Note: H_2 flow rate for all runs = 48 cm^3/min ≈ 6.9 A ≈ 1.1 A/cm^2.
*Run 10 was conducted with pure oxygen.
**Results not provided because of manuscript length considerations.

11–16 were conducted to evaluate the effect of air flow rate and extent of air stream humidification. In runs 17–22, air flow rate and cathode humidification studies were repeated at a higher cell and anode sparger temperature. Runs 23, 24, and 25 in conjunction with runs 12 and 18 were used to determine the effect of increase in cell temperature with and without a corresponding increase in the anode sparger temperature. As explained in the first part of this series, in between each run, the MEA was removed from the cell assembly and subjected to an overnight drying process under a lamp and fan to provide the same starting point for each experiment in terms of membrane hydration and water content in the electrodes.

The electrode segments were then subjected to a liquid water "load-up " step, wherein they were simultaneously discharged at a constant current of 100 mA for 1 h. This step was included in the experimental scheme to rehydrate the MEA that was dried overnight. The constant current discharge was also expected to provide uniform water accumulation in all the segments along the channel length. Hydrogen and oxygen flow rates and sparger temperatures used in this load-up step were the same as in the massage experiments. After the constant current step, the gas feed to the cathode was switched to air and gas flow rates and sparger temperatures were adjusted to the desired values. The segments were then held simultaneously at a constant voltage of 0.45 V for 4 h, and the current response was recorded over time. In all the runs presented in this study, the hydrogen flow rate was well in excess of the reaction demand.

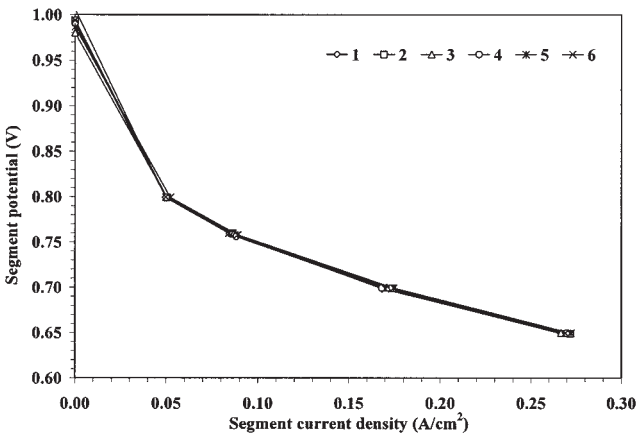

Figure 2. Polarization curves from run 10 for six segments in MEA 3.

H_2 flow rate = 48 cm^3/min (6.9 A or 1.1 A/cm^2), O_2 flow rate = 19 cm^3/min (5.5 A or 0.87 A/cm^2), H_2 humidifier temperature = 40°C, O_2 humidifier temperature = 30°C, and cell temperature = 27–28°C.

Results and Discussion

Effect of air flow rate and air stream humidification

Figures 3–6 provide the current responses of the six segments held at 0.45 V over a period of 4 h, obtained from runs 11, 12, 13, and 14, respectively. All relevant operating parameters except air flow rate were maintained constant in these runs (see Table 1). As seen in Figure 3, at a low air flow rate of 16.6 cm^3/min (1.0 A), the local current density distribution along the length of the channel was dominated by the available oxygen concentration along the channel. At segment 1, which was closest to the inlet where the oxygen concentration was the highest, the local current density was the greatest. As oxygen was consumed along the length of the channel, the oxygen concentration decreased down the channel, resulting in a drop in the reaction rate or current density in segments downstream. Also, at the beginning of the experiment, current densities at segments 1 and 2 were 0.34 and 0.27 A/cm^2, respectively, which gradually dropped within 50 min of discharge and stabilized at about 0.28 and 0.18 A/cm^2, respectively. Correspondingly segments 3 through 6 started out lower and registered an increase over this time. At the beginning of the experiment the inlet segments that were not limited by oxygen availability were also relatively dry and were able to sustain higher currents. However, over time, water accumulation in the electrode resulted in a slight reduction in performances of these segments near the inlet. This drop in current density over time at segments 1 and 2 resulted in higher oxygen concentration downstream that improved the performance over the initial 50

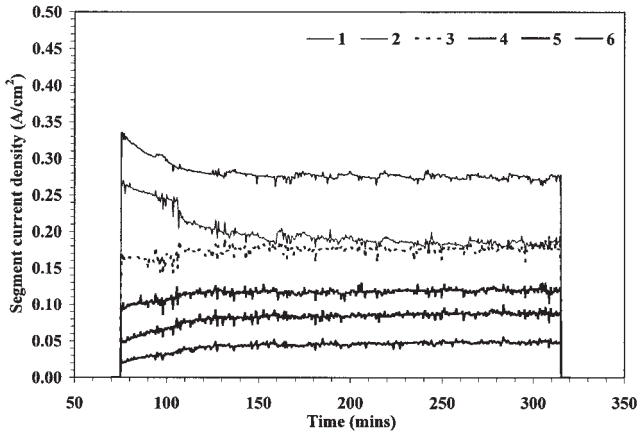

Figure 3. Individual segment current response to an imposed voltage of 0.45 V obtained from run 11 (segment potentials controlled independently).

H_2 flow rate = 48 cm^3/min (6.9 A or 1.1 A/cm^2), air flow rate = 16.6 cm^3/min (1.0 A or 0.16 A/cm^2), H_2 humidifier temperature = 40°C, air humidifier temperature = 30°C, and cell temperature = 27–28°C.

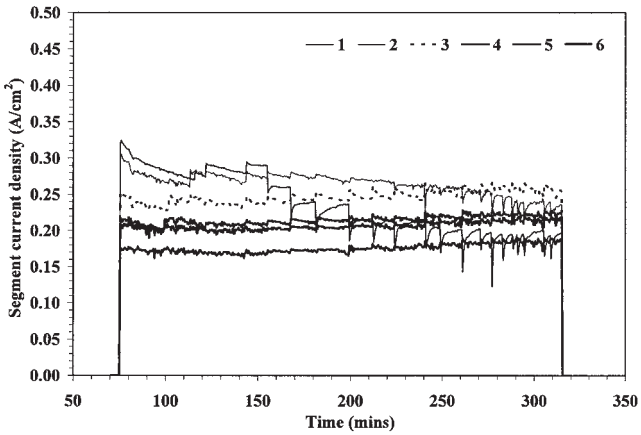

Figure 5. Individual segment current response to an imposed voltage of 0.45 V obtained from run 13 (segment potentials controlled independently).

H_2 flow rate = 48 cm^3/min (6.9 A or 1.1 A/cm^2), air flow rate = 35.8 cm^3/min (2.15 A or 0.34 A/cm^2), H_2 humidifier temperature = 40°C, air humidifier temperature = 30°C, and cell temperature = 27–28°C.

min of segments 3, 4, 5, and 6 that were limited by oxygen availability.

As the air flow rate was increased to 22 cm^3/min (1.32 A) as in run 12, represented by Figure 4, the performance of downstream segments improved as a result of the greater availability of oxygen. As expected, the current density at segment 1 that was receiving plenty of oxygen even at the lower flow rate, was practically unaffected by the increase in the flow rate. Figure 4 also indicates a drop in the current densities at segments 1 and 2 toward the end of the experiment. Further increases in the air flow rate to 36 and 47.5 cm^3/min (runs 13 and 14, respectively), as represented in Figures 5 and 6, resulted in additional increases in the current density at downstream segments, whereas the current response at segment 1 remained relatively constant. For the sake of comparison, the ranges of current density along the channel length at the beginning of the experiments were (inlet–exit) 0.34–0.02, 0.32–0.1, 0.33–0.17, and 0.35–0.22 A/cm^2 for runs 11 through 14, respectively. As in run 11 all the experiments at higher air flow rates exhibited an initial drop in the current density at segments 1 and 2 over the first 50 min. However, at higher gas flow rates, the current density at these segments continued to decrease over the entire course of the experiment. The rate of this drop increased with increasing air flow rate, leading to lower current densities at segments 1 and 2 toward the end of the experiment. Besides the condensation effects arising from the slight temperature difference (2°C) between the air sparger and the cell, we also believe that at higher flow rates, liquid water entrainment in the gas stream at the air sparger became substantial. This resulted in significant presence of liquid water in the channel near the inlet, which

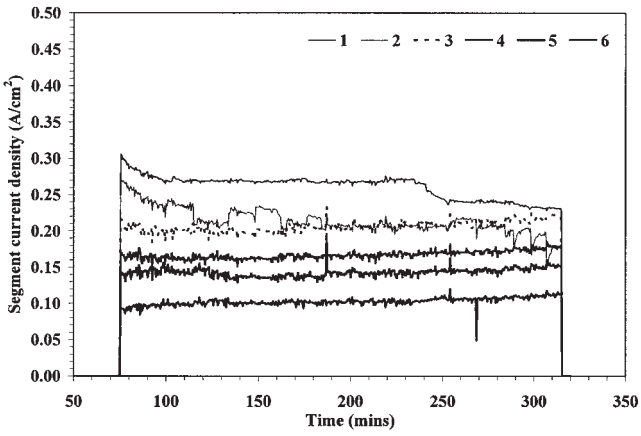

Figure 4. Individual segment current response to an imposed voltage of 0.45 V obtained from run 12 (segment potentials controlled independently).

H_2 flow rate = 48 cm^3/min (6.9 A or 1.1 A/cm^2), air flow rate = 22 cm^3/min (1.32 A or 0.21 A/cm^2), H_2 humidifier temperature = 40°C, air humidifier temperature = 30°C, and cell temperature = 27–28°C.

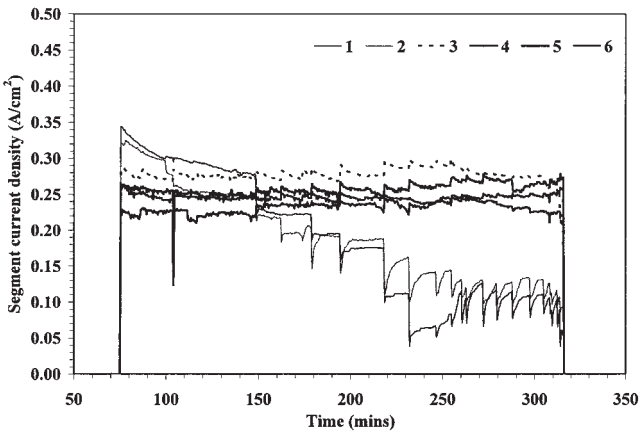

Figure 6. Individual segment current response to an imposed voltage of 0.45 V obtained from run 14 (segment potentials controlled independently).

H_2 flow rate = 48 cm^3/min (6.9 A or 1.1 A/cm^2), air flow rate = 47.5 cm^3/min (2.85 A or 0.45 A/cm^2), H_2 humidifier temperature = 40°C, air humidifier temperature = 30°C, and cell temperature = 27–28°C.

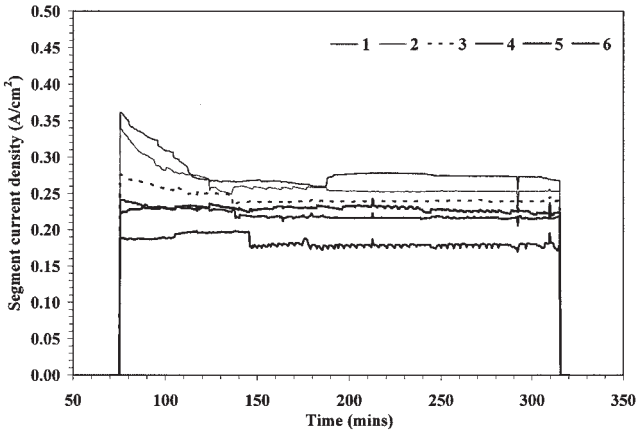

Figure 7. Individual segment current response to an imposed voltage of 0.45 V obtained from run 15 (segment potentials controlled independently).

H_2 flow rate = 48 cm^3/min (6.9 A or 1.1 A/cm^2), air flow rate = 47.5 cm^3/min (2.85 A or 0.45 A/cm^2), H_2 humidifier temperature = 40°C, no air humidifier, and cell temperature = 27–28°C.

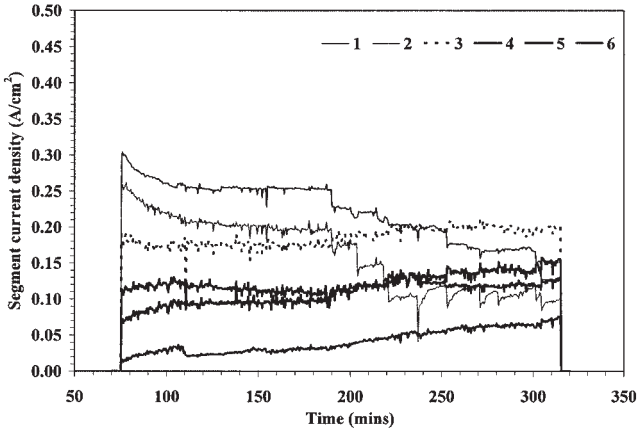

Figure 8. Individual segment current response to an imposed voltage of 0.45 V obtained from run 16 (segment potentials controlled independently).

H_2 flow rate = 48 cm^3/min (6.9 A or 1.1 A/cm^2), air flow rate = 16.6 cm^3/min (1.0 A or 0.16 A/cm^2), H_2 humidifier temperature = 40°C, air humidifier temperature = 45°C, and cell temperature = 27–28°C.

ultimately resulted in water accumulation and flooding in the electrodes corresponding to segments 1 and 2. To verify this hypothesis, run 15 was conducted without a sparger for the air stream while keeping all other operating parameters similar to run 14, and the results are provided in Figure 7. When the sparger was removed, segments 1 and 2 did not register a decrease in current densities beyond the initial drop over the first 50 min and remained constant over the rest of the experiment, confirming our suspicions about water entrainment in the sparger at higher flow rates.

Moreover, in runs 12 through 14, the gain in oxygen concentration downstream arising from the decrease in performance at the inlet at any time was not as significant as that in run 11 because of the higher air flow rates used in the latter runs. Thus, downstream segments did not register a significant improvement in performance. Figure 8 provides the results from run 16, conducted under conditions similar to those of run 11 (air flow rate of 16.6 cm^3/min), except for the air sparger temperature that was increased from 30 to 45°C. It is evident from Figures 3 and 8 that the initial performances of the segments are similar between the two runs. However, for the case with the higher air sparger temperature, the performance of segments 1 and 2 started to decline further during the course of the experiment as a result of condensation of water near the inlet, resulting in a net reduction in the water removal rate from these electrodes. Unlike runs 12 through 14, because of the low air flow rate, this drop in current density at the inlet resulted in more oxygen being available for downstream segments, leading to a considerable sustained increase in their performances. Thus in run 16, the initial peak observed at segment 1 in the current density profile along the channel shifted away from the inlet toward segment 3 during the course of the experiment as a result of electrode flooding effects and consequent increase in downstream oxygen concentration.

The results from the six experiments discussed above are also summarized as total cell current density (average of six segments) vs. time in Figure 9. It is clear from Figure 9 that increasing air flow rate resulted in better utilization of the reactive area that is further downstream from the inlet, leading to a more uniform local current density distribution that yielded a higher average cell current density. At sufficiently high air flow rates, however, gains from better utilization were offset by losses arising from water accumulation at the inlet caused by condensation and liquid water entrainment in the gas stream at the cathode sparger. This observation has implications when air stream humidification is implemented by liquid water injection. The fraction of the supplied oxygen that was consumed was about 92, 83, 64, and 50% for air flow rates of 1, 1.32, 2.15, and 2.85 A (corresponding to 0.16, 0.21, 0.34, 0.45 A/cm^2) equivalent. In terms of practical applications involving air operation, there seems to be a trade-off between achieving uniformity in current density distribution and reactant utilization. Other than a shift in the location of the peak current density, Figure 9 also

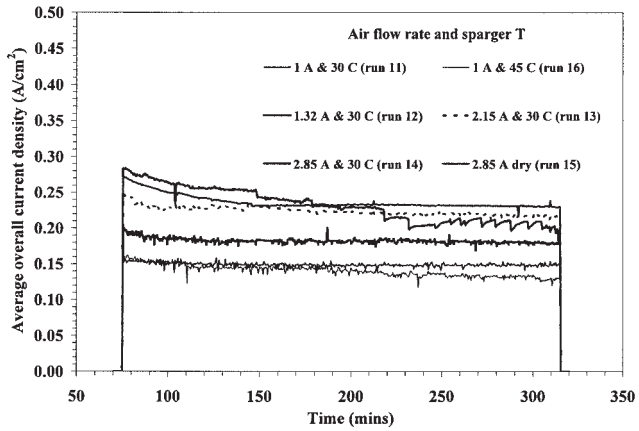

Figure 9. Effect of air flow rate and air sparger temperature on the average cell current density with individual segment potentials controlled independently at 0.45 V (runs 11 through 16).

H_2 flow rate = 48 cm^3/min (6.9 A or 1.1 A/cm^2), H_2 humidifier temperature = 40°C, and cell temperature = 27–28°C.

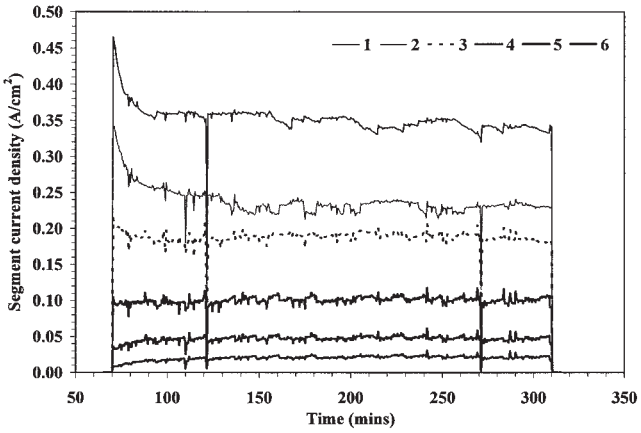

Figure 10. Individual segment current response to an imposed voltage of 0.45 V obtained from run 17 (segment potentials controlled independently).

H_2 flow rate = 48 cm^3/min (6.9 A or 1.1 A/cm^2), air flow rate = 16.6 cm^3/min (1.0 A or 0.16 A/cm^2), H_2 humidifier temperature = 60°C, air humidifier temperature = 30°C, and cell temperature = 44–46°C.

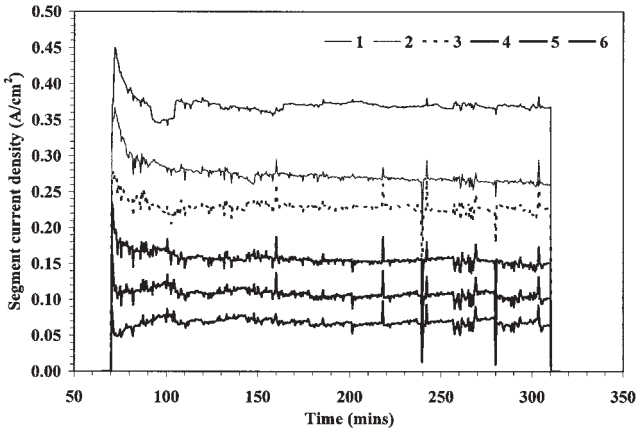

Figure 11. Individual segment current response to an imposed voltage of 0.45 V obtained from run 18 (segment potentials controlled independently).

H_2 flow rate = 48 cm^3/min (6.9 A or 1.1 A/cm^2), air flow rate = 22 cm^3/min (1.32 A or 0.21 A/cm^2), H_2 humidifier temperature = 60°C, air humidifier temperature = 30°C, and cell temperature = 44–46°C.

indicates a slight loss in overall performance between runs 11 and 16 where the air sparger temperature was increased from 30 to 45°C. The drop in the average cell current density indicates that the losses at the inlet segments as a result of flooding were not completely compensated by the oxygen concentration related gain at the downstream segments.

The effect of air flow rate and cathode sparger temperature was also investigated at a higher cell temperature (44–46°C) and hydrogen sparger temperature (60°C). Except for the cell and anode sparger temperatures, runs 17 through 19 were conducted under conditions similar to those of runs 11 through 13 (corresponding to increasing air flow rates of 16.6, 22, and 36 cm^3/min), and the results from these experiments are provided in Figures 10–12, respectively. These results are comparable to the lower temperature runs and validate the inferences drawn in the previous sections. The main similarity between these runs and the set of experiments at lower temperature was that increasing air flow rates resulted in more oxygen availability over the reaction area downstream, thereby resulting in an increase in the local current densities at segments further down the channel. There are indeed other significant differences between these two groups of experiments that can be primarily attributed to the higher cell temperature and are discussed in detail in later sections.

Runs 20 through 22 were conducted at the intermediate air flow rate of 22 cm^3/min, whereas the air sparger temperature was maintained at 50, 60, and 75°C, respectively. Increasing the air sparger temperature to 50 and 60°C did not have a significant effect on the current density profile along the channel, and thus results from runs 20 and 21 are not presented here for the sake of brevity. A further increase in the sparger temperature to 75°C (run 22) resulted in a pronounced effect on the current density distribution, as shown in Figure 13. Because of the drastic difference in the air sparger and cell temperatures, considerable condensation of water vapor occurred near the inlet, leading to severe flooding of the electrode at segment 1 within a few minutes of discharge. Upon comparing Figures 11 and 13 it is evident that subsequent segments benefited from the drop in oxygen consumption at segment 1 as a result of flooding. The results from runs 17, 18, 19, and 22 are also provided in Figure 14 as the average cell current density over time. On comparing the overall performances in runs 18 and 22, it is clear that the loss in performance at segment 1 as a result of flooding is significantly more dominant than the gains exhibited by the latter segments, leading to a net reduction in the overall performance stemming from increasing the air sparger temperature to 75°C.

A major feature observed in experiments that involved a significant presence of liquid water in the channel (runs 13, 14, 16, and 22) is the oscillatory behavior exhibited by electrodes

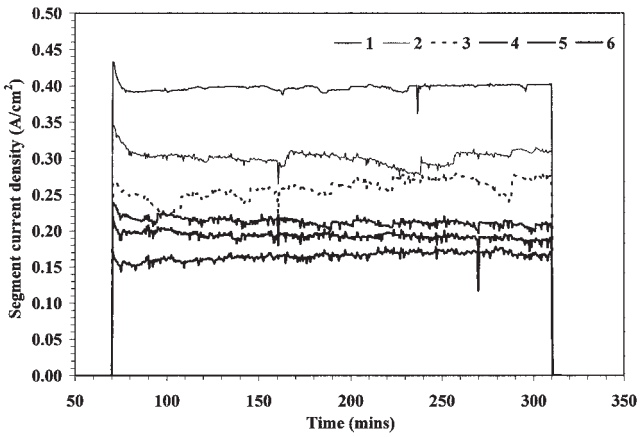

Figure 12. Individual segment current response to an imposed voltage of 0.45 V obtained from run 19 (segment potentials controlled independently).

H_2 flow rate = 48 cm^3/min (6.9 A or 1.1 A/cm^2), air flow rate = 35.8 cm^3/min (2.15 A or 0.34 A/cm^2), H_2 humidifier temperature = 60°C, air humidifier temperature = 30°C, and cell temperature = 44–46°C.

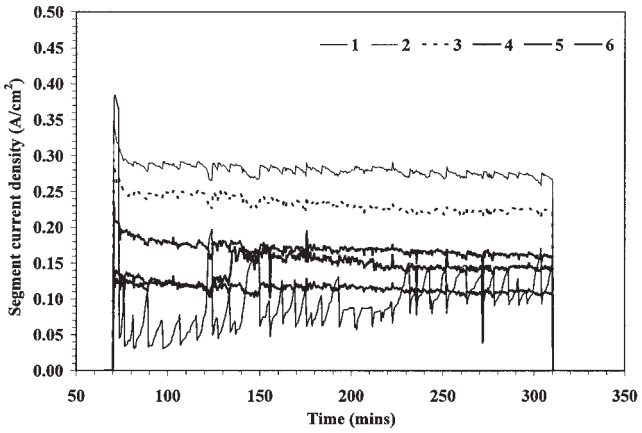

Figure 13. Individual segment current response to an imposed voltage of 0.45 V obtained from run 22 (segment potentials controlled independently).

H_2 flow rate = 48 cm^3/min (6.9 A or 1.1 A/cm^2), air flow rate = 22 cm^3/min (1.32 A or 0.21 A/cm^2), H_2 humidifier temperature = 60°C, air humidifier temperature = 75°C, and cell temperature = 44–46°C

that were flooded (mainly at segments 1 and 2). In all these runs, the flooding electrode oscillated between sharp drops in performance and a gradual recovery. We hypothesize that this phenomenon is probably related to accumulation of liquid water in the void volumes associated with the fittings and machined gas conduits. Once this volume was filled up, a bead of water is transported along the length of the channel, wetting the electrode channel interface along the way. Based on this hypothesis, the sharp drops correspond to the wetting of the interface that lead to a net reduction in the available gas transport area. The electrode then recovers gradually in the time it takes for the channel-inlet void volume to fill up again. However, this phenomenon is observed only at the segments close to the inlet. One possible reason for this may be that the effect of a moving bead on the transport rate of reactant gas to the catalyst layer is minimal relative to that of bead accumulation. Interestingly, the frequency of these oscillations was greater when the difference between the sparger and cell temperatures was greater (comparing runs 14 and 16). Large temperature differences result in a greater rate of water condensation and thus accumulation, leading to more frequent bead transport along the channel.

This kind of an oscillatory behavior in PEM fuel cells has so far not been reported in the literature. Transient data on PEM fuel cells, available in the literature, are usually based on cells with much larger reactive area using flow fields with multiple gas channels. When multiple gas channels are involved, water accumulation in a single gas channel and its effect on a localized region are masked in the overall performance of the cell. This masking effect is evidenced even in single-channel experiments, as shown by the data obtained from run 22. In this run the flooded electrode at segment 1 showed oscillations (see Figure 13) in current density ranging over 0.1A/cm^2. However, these oscillations are not reflected in the overall current density for this run shown in Figure 14 because the electrode at segment 1 is only a fraction of the total reactive area. More experiments and detailed analysis are needed to address the question of whether the oscillatory phenomenon observed here that is associated with water accumulation in the void volumes of the channel has relevance to practical applications or is just an experimental artifact. Larger cells with multiple gas channels are needed for such experiments where segmentation of the electrode and current collector is applied at the single-channel level.

Effect of temperature and anode humidification

The two groups of experiments—runs 11 through 13 and 17 through 19—can also be compared to observe the effect of cell temperature on the local current density measurements. The two sets of experiments were conducted at a cell temperature of 30 and 45°C, respectively, with a corresponding anode sparger temperature of 40 and 60°C. Given that the focus of these experiments was to examine the effect of improved kinetics and water removal at the cathode resulting from elevation in temperature, the anode humidification level was increased in the latter set of experiments to avoid dehydration effects in the current density pattern. Based on the results provided in Figures 3 and 10, corresponding to runs conducted at a low air flow rate of 16.6 cm^3/min (1 A), increasing cell temperature resulted in a significant increase in the current densities at the first three segments, whereas the latter segments registered a decrease. Sufficient oxygen was available at segments 1, 2, and 3 to reflect the increase in reaction rate resulting from enhanced kinetics and greater water removal capacity achieved through an increase in temperature. However, the performance-limiting criteria for latter segments was the availability of oxygen. The enhancement in kinetics, and water evaporation at higher temperature—were offset by the more pronounced lack of oxygen, especially given the higher reaction rates near the channel entrance. This actually led to a drop in the current densities with increasing temperature at segments downstream. Essentially, increasing the cell temperature led to a greater gradient in the current density profile along the channel at low air flow

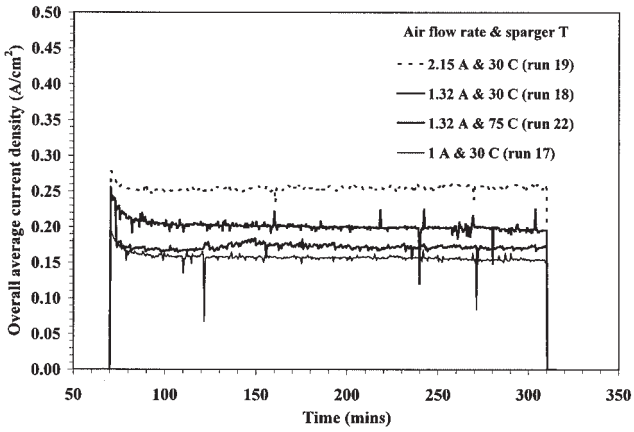

Figure 14. Effect of air flow rate and air sparger temperature on the average cell current density with individual segment potentials controlled independently at 0.45 V, at higher cell temperature (runs 17, 18, 19, and 22).

H_2 flow rate = 48 cm^3/min (6.9 A or 1.1 A/cm^2), H_2 humidifier temperature = 60°C, and cell temperature = 44–46°C.

rates. A similar phenomenon was observed at the next flow rate of 22 cm^3/min (1.32 A) (see Figures 4 and 11). Upon further increasing the flow rate (Figures 5 and 12), the kinetic and mass transport and water removal benefits of operating at a higher temperature started to reflect in the downstream segment current densities (based on the first 1.5 h of discharge).

A couple of other inferences can also be drawn based on the results from these six experiments where the cathode sparger temperature was held constant at 30°C. As mentioned earlier in the low cell temperature experiments, increasing the flow rate did not affect the performance of the first segment, whereas at higher cell temperatures, the steady-state performance of segment 1 actually improved noticeably with increasing air flow rate. By increasing the cell temperature while keeping the cathode sparger at 30°C, greater evaporation capacity was imparted to the air stream that helped minimize the water accumulation within the electrode near the inlet and its adverse effects. This is also the reason for not observing the water entrainment/condensation related flooding of segments 1 and 2 in the higher cell temperature runs. Finally, based on the overall cell performances summarized in Figure 14, at higher cell temperature (and corresponding increase in anode humidity), the percentage consumption rates of the oxygen available in the supplied air stream were 95, 90, and 75%, respectively, for the three different air flow rates involved in runs 17 through 19. As expected, these values are greater than those reported for the low-temperature experiments because of an increase in reaction kinetics and improvement in water removal achieved at higher cell temperature.

Runs 23, 24, and 25 were conducted to examine the effect of cell temperature coupled with dehydration effects at the anode. In run 23 the segments were discharged at a cell temperature of 45°C with the anode sparger temperature reduced back to 40°C. Air was supplied at the rate of 22 cm^3/min. The results are provided in Figure 15. The significant influence of anode hydration level is evident from comparing Figures 11 and 15. Because of the lack of sufficient humidification at the anode,

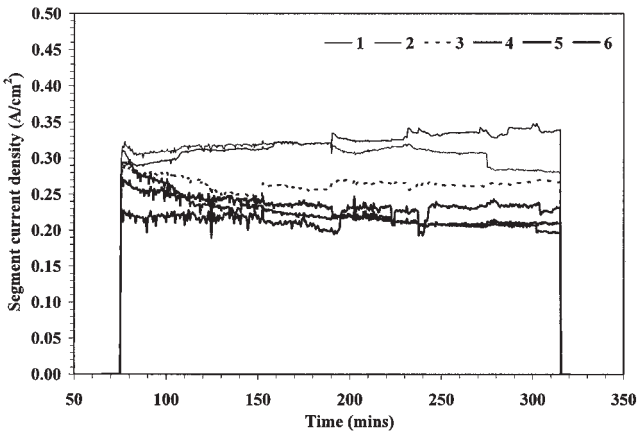

Figure 15. Individual segment current response to an imposed voltage of 0.45 V obtained from run 23 (segment potentials controlled independently).

H_2 flow rate = 48 cm^3/min (6.9 A or 1.1 A/cm^2), air flow rate = 22 cm^3/min (1.32 A or 0.21 A/cm^2), H_2 humidifier temperature = 40°C, air humidifier temperature = 30°C, and cell temperature = 44–46°C.

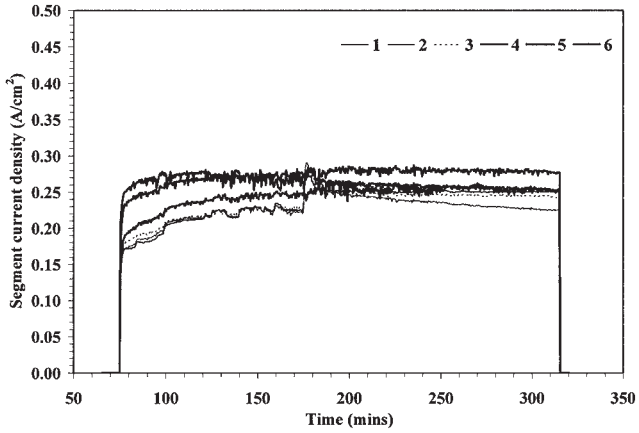

Figure 16. Individual segment current response to an imposed voltage of 0.45 V obtained from run 24 (segment potentials controlled independently).

H_2 flow rate = 48 cm^3/min (6.9 A or 1.1 A/cm^2), air flow rate = 22 cm^3/min (1.32 A or 0.21 A/cm^2), H_2 humidifier temperature = 40°C, air humidifier temperature = 30°C, and cell temperature = 54–56°C.

the initial performances of the first three segments are much lower in run 23 than those in run 18. This led to an improvement in the current densities at segments 4, 5, and 6 as a result of greater oxygen availability at the initial stages of discharge. The current spread along the channel in this case was <0.1 A/cm^2, compared to a spread of >0.3 A/cm^2 observed in run 18. Over the course of the experiment, the product water helped in the humidification of the segments near the inlet, leading to a slight improvement in their performance, which ultimately resulted in increasing the current spread to about 0.14 A/cm^2.

Run 24 was conducted at an even higher cell temperature of 55°C with the anode sparger held at 40°C and the same air flow rate as before. The segment current densities are provided in Figure 16. By increasing the cell temperature further, while maintaining the anode sparger temperature at 40°C, the dehydration effects became more severe. During the initial periods of discharge, the dehydration effect was severe enough to dramatically reduce the current densities along the entire length of the channel. At the initial stages, however, the decreasing profile of the local current density was preserved along the channel as the inlet segments still benefited from what little humidity was available in the anode stream. Over time, the product water helped humidification at all the segments, leading to an increase in current density along the entire length of the channel. The current density spread toward the end of the experiment was about 0.05 A/cm^2. Given the relatively low air flow rates used in this run and the elevated temperature, the lower spread in current densities suggests dehydration as the dominant factor that determined the spatiotemporal distribution of local current densities.

To confirm these dehydration effects, run 25 was conducted under conditions similar to those of the previous run with an elevated anode sparger temperature of 75°C. The results from this final experiment are provided in Figure 17. A comparison of the initial local current density distribution provided in Figures 16 and 17 indicates that increasing the anode sparger temperature helped in humidification along the entire length of

the channel. Also, over the course of discharge, the greater moisture content provided to the anode better aided the process of in situ humidification by product water, leading to a current density spread that was more influenced by the oxygen concentration profile rather than the dehydration pattern. Figure 18 provides the average cell current densities over time from runs 12, 18, 23, 24, and 25 that summarize the effect of cell temperature and anode humidification at constant air flow rate of 22 cm^3/min (1.32 A). At lower anode sparger temperature, it can be seen from Figure 18 that increasing the cell temperature from 28 to 45°C resulted in an improvement in the average current density because of improvement in kinetics and water removal by evaporation. Further increase in the cell temperature resulted in dehydration of the anode that influenced the performance during the early stages of discharge. Eventually the product water helped in the humidification process, leading to better reactant utilization over time. When the anode sparger temperature was correspondingly increased along with the cell temperature, higher reaction rates (current densities) and thus utilization was achieved over the entire course of the experiment. The fact that the average current densities in runs 23 and 25 are the same despite a significant increase in both the cell and anode sparger temperatures suggests that the fuel cell performance is limited at the cathode because of oxygen diffusion limitations and availability.

Conclusions

The effects of cell temperature, humidification of the anode and cathode gas streams, and oxidant flow rate on the spatial and temporal current density distribution in a single-channel PEM fuel cell operated on air and hydrogen were investigated using a segmented electrode/current collector setup. Related studies on pure oxygen operation and hydrogen starvation effects are presented in the first article of this series.

The local current density distribution along the channel was studied over 4 h at various oxygen flow rates of 16.6, 22, 35.8, and 47.5 cm^3/min corresponding to 0.16, 0.21, 0.34, and 0.45 A/cm^2, at two different cell temperatures of 28 and 30°C with a corresponding anode sparger temperature of 40 and 60°C. The effect of the cathode sparger temperature was also investigated. The current density distribution was strongly influenced by the availability of oxygen along the length of the channel. Increasing flow rates yielded greater current densities at downstream segments. Higher air flow rates and greater cathode humidification resulted in flooding at segments near the inlet because of liquid water entrainment in the air stream and condensation.

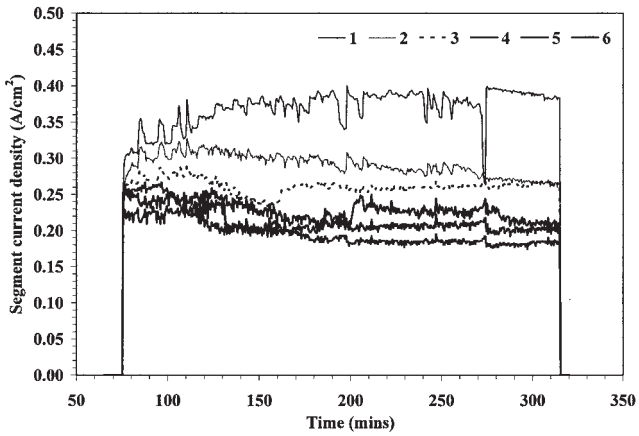

Figure 17. Individual segment current response to an imposed voltage of 0.45 V obtained from run 25 (segment potentials controlled independently).

H_2 flow rate = 48 cm^3/min (6.9 A or 1.1 A/cm^2), air flow rate = 22 cm^3/min (1.32 A or 0.21 A/cm^2), H_2 humidifier temperature = 75°C, air humidifier temperature = 30°C, and cell temperature = 54–56°C.

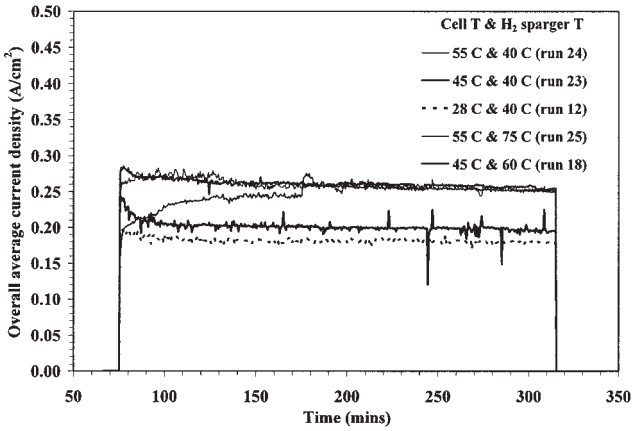

Figure 18. Effect of cell temperature and hydrogen sparger temperature on the average cell current density with individual segment potentials controlled independently at 0.45 V (runs 12, 18, 23, 24, and 25).

H_2 flow rate = 48 cm^3/min (6.9 A or 1.1 A/cm^2), air humidifier temperature = 30°C.

At lower air flow rates, when elevation in cell temperature was accompanied by an increased level of anode humidification, an improvement in the current density at the first three segments was observed that resulted in a loss in performance downstream. By increasing air flow rate, effects of higher kinetics and water removal rate brought about by increasing the cell temperature were ultimately observed at all segments over the entire length of the channel. When anode humidification levels were not increased at higher cell operating temperatures, the spatiotemporal current density distribution was primarily influenced by the dehydration pattern in the segmented fuel cell assembly. Given the chosen operating segment potential of 0.45 V, beyond a point, oxidant availability and diffusion limitations at the cathode tended to dominate the current density pattern along the channel and further increases in the cell temperature and anode humidification had minimal effect.

As a concluding remark, although this study is quite elaborate in addressing local current density mapping at various operational aspects of PEM fuel cells, a major limitation of this work is the lack of data at cell temperatures > 55°C. Although many portable PEM fuel cells applications may fall within this limit, other important applications such as transportation require operating temperatures in the range of 70 to 80°C. Concerns regarding contact resistance artifacts arising from loss in surface smoothness of the segmented current collector assembly as a result of the drastic difference in the thermal expansion

coefficient of acrylic and graphite limited this study to moderate temperatures. Although one would expect qualitatively similar results at higher temperatures, actual experimentation at 60 to 80°C is essential, especially given the exponential dependency7 of water vapor pressure on temperature. The saturation pressure of water is crucial in deciding the relative dominance of the two water-removal mechanisms: evaporation and liquid water transport by capillarity. Segmented fuel cell assembly with negligible differences in component thermal expansion coefficients is needed for this. One possible approach would be to embed graphite current collector strips coated with thin insulation (electronic) in a block of graphite instead of acrylic. Other noncorroding electrically conductive materials such as stainless steel or gold-coated copper strips can also be used.

Acknowledgments

This work was supported by the National Science Foundation under Grant CTS-9910923.

Literature Cited

1. Springer TE, Wilson MS, Gottesfeld S. Modeling and experimental diagnostics in polymer electrolyte fuel cells. *J Electrochem Soc*. 1993; 140:3513-3526.
2. Bernardi DM, Verbrugge MW. A mathematical model of the solid-polymer-electrolyte fuel cell. *J Electrochem Soc*. 1992;139:2477-2491.
3. Nguyen TV, White RE. A water and heat management model for proton-exchange-membrane fuel cells. *J Electrochem Soc*. 1993;140: 2178-2186.
4. West AC, Fuller TF. Influence of rib spacing in proton-exchange membrane electrode assemblies. *J Applied Electrochem*. 1996;26:557-565.
5. Gurau V, Liu H, Kakac S. Two-dimensional model for proton exchange membrane fuel cells. *AIChE J*. 1998;44:2410-2422.
6. Shimpalee S, Dutta S. Numerical prediction of temperature distribution in PEM fuel cells. *J Numer Heat Transfer*. 2000;38:111-128.
7. Natarajan D, Nguyen TV. A two-dimensional, two-phase, multi-component, transient model for the cathode of a proton exchange membrane fuel cell using conventional gas distributors. *J Electrochem Soc*. 2001;148:1324-1335.
8. Natarajan D, Nguyen TV. Three-dimensional effects of liquid water flooding in the cathode of a PEM fuel cell. *J Power Sources*. 2003; 115:66-80.
9. Yi JS, Nguyen TV. An along-the-channel model for proton exchange membrane fuel cells. *J Electrochem Soc*. 1998;145:1149-1159.
10. He W, Yi JS, Nguyen TV. Two-phase flow model of the cathode of PEM fuel cells using interdigitated flow fields. *AIChE J*. 2000;46: 2053-2064.
11. Wang ZH, Wang CY, Chen KS. Two-phase flow and transport in the air cathode of proton exchange membrane fuel cells. *J Power Sources*. 2001;94:40-50.
12. Cleghorn SJC, Derouin CR, Wilson MS, Gottesfeld S. A printed circuit board approach to measuring current distribution in a fuel cell. *J Appl Electrochem*. 1998;28:663-672.
13. Stumper J, Campbell SA, Wilkinson DP, Johnson MC, Davis M. In-situ methods for the determination of current distribution in PEM fuel cells. *Electrochim Acta*. 1998;43:3773-3783.
14. Wieser Ch, Helmbold A, Gulzow E. A new technique for two-dimensional current distribution measurements in electrochemical cells. *J Appl Electrochem*. 2000;30:803-807.
15. Brett DJL, Atkins S, Brandon NP, Vesovic V, Vasileiadis N, Kucernak AR. Measurement of the current distribution along a single flow channel of a solid polymer fuel cell. *Electrochem Commun*. 2001;3: 628-632.
16. Mench MM, Wang CY. An in situ method for determination of current distribution in PEM fuel cells applied to a direct methanol fuel cell. *J Electrochem Soc*. 2003;150:A79-A85.
17. Mench MM, Wang CY. In situ current distribution measurements in polymer electrolyte fuel cells. *J Electrochem Soc.* 2003;150:A1052-A1059.
18. Nopenen M, Mennola T, Mikkola M, Hottinen T, Lund P. Measurement of current distribution in a free-breathing PEMFC. *J Power Sources*. 2002;106:304-312.
19. Hottinen T, Nopenen M, Mennola T, Himanen O, Mikkola M, Lund P. Effect of ambient conditions on performance and current distribution of a polymer electrolyte membrane fuel cell. *J Appl Electrochem*. 2003;33:265-271.
20. Bender G, Wilson MS, Zawodzinski TA. Further refinements in the segmented cell approach to diagnosing performance in polymer electrolyte fuel cells. *J Power Sources*. 2003;123:163-171.
21. Natarajan D, Nguyen TV. Effect of electrode configuration and electronic conductivity on current density distribution measurements in PEM fuel cells. *J Power Sources*. 2004;135:95-109.

Manuscript received Jun. 9, 2004, revision received Feb. 2, 2005, and final revision received May 2, 2005.